Vacuum Steered-Electron Electric-Field Sensor

Kirt R. Williams, *Senior Member, IEEE,* Dirk P. H. De Bruyker, *Member, IEEE,* Scott J. Limb, Eric M. Amendt, *Member, IEEE,* and Doug A. Overland

***Abstract*—In a new type of microelectromechanical system (MEMS) electric-field sensor, a sheet of electrons is thermionically emitted by a hot cathode, flows through a vacuum, and is collected by a pair of anodes 2000 μm away. As the electrons move through the vacuum, they are steered by external electric fields, resulting in a differential current at the anodes. The micromachined tungsten cathode has a low-work-function coating and is suspended over a cavity on a glass chip. These sensors have been operated both in a vacuum chamber and sealed in glass vacuum tubes. Measured sensitivities in a vacuum tube at 10, 100, and 1000 Hz are 470, 230, and 140 mV/m $\cdot$ Hz$^{1/2}$, respectively; sensitivities in a vacuum chamber at the same frequencies are 34, 6.3, and 2.4 mV/m $\cdot$ Hz$^{1/2}$, respectively. [2013–0021]**

***Index Terms*—MEMS, electric field, sensor, vacuum, electron beam.**

I. Introduction

THERE is a need for low-size, -weight, and -power (low-SWaP), low-frequency electric-field sensors. Applications include long-distance detection and avoidance of power lines (at 50 or 60 Hz) by helicopters and unmanned aerial vehicles (UAVs), noncontact monitoring of heart voltages or fields (electrocardiograms, or ECGs), and brain electric activity (electroencephalograms, or EEGs).

A. Antennas Versus Sensors

Electric-field detectors can be usefully divided into two types: 1) antennas, which typically have a size of 1/10 of a wavelength to a full wavelength and pick up high-frequency electromagnetic radiation far from the source; and 2) sensors, which have sizes much smaller than a wavelength and can pick up low-frequency fields in either the near zone or far zone [1]. The division between low and high frequencies can be somewhat arbitrarily set at 100 kHz. In this section, we concentrate on the sensors.

Manuscript received January 15, 2013; revised May 6, 2013; accepted May 6, 2013. This work was supported by the Defense Advanced Research Projects Agency Microsystems Technology Office E-FED program under Contract HR0011-10-C-0046. The views and conclusions contained in this paper are those of the authors and should not be interpreted as representing the official policies, either expressly or implied, of DARPA or the U.S. Government. Subject Editor A. J. Ricco.

K. R. Williams was with Science Applications International Corporation, San Diego, CA 92121 USA. He is now with InvenSense, San Jose, CA 95110 USA (e-mail: kirt_williams@ieee.org).

D. P. H. De Bruyker and S. J. Limb are with the Palo Alto Research Center, Palo Alto, CA 94304 USA (e-mail: dirk.debruyker@parc.com; scott.limb@parc.com).

E. M. Amendt and D. A. Overland are with Science Applications International Corporation, San Diego, CA 92121 USA (e-mail: eric.m.amendt@saic.com; doug.a.overland@saic.com).

Color versions of one or more of the figures in this paper are available online at http://ieeexplore.ieee.org.

Digital Object Identifier 10.1109/JMEMS.2013.2262924

B. Existing Electric-Field Sensors

All low-frequency electric-field sensors found in the literature with at least moderate sensitivity (on the order of 1 V/m $\cdot$ Hz$^{1/2}$) have been one of two types: 1) high-impedance voltmeters connected to plates some distance apart, where the electric field $E = cV/d$, where V is the voltage and d is the distance, reduced slightly by a coupling factor c; or 2) various electro-optic sensors.

Krupka *et al.* of QUASAR have built a voltmeter-type sensor with plates 330 mm apart and a coupling factor of 0.4 [2]. The plate spacing can be reduced to any value, but the coupling factor is reduced. As built, it is extremely sensitive, at 2 μV/m $\cdot$ Hz$^{1/2}$ at 100 Hz [2]. Its size is too large for many applications, including forming a sensor array for EEGs and for use on a UAV.

SRICO has a commercial product using photonic crystals formed in thin films of $LiNbO_3$ in a Mach–Zehnder interferometer [3], [4]. It has a sensitivity of 0.1 mV/m $\cdot$ Hz$^{1/2}$ from 10 Hz to 1 GHz, with a minimum field strength of 10 V/m. The sensor chip is mounted in a 50-mm-long housing, coupled to optical fibers. It requires a high-power (up to 40 mW) tunable laser, which in turn needs tens of watts of input power, making it incompatible with low-SWaP applications.

II. Steered-Electron Electric-Field Sensor Overview

A. Operation

The steered-electron electric-field (SEEF) sensor is based on the simple concept of an external electric field deflecting a beam of electrons. A higher current in the beam is desirable because it produces a better signal-to-noise (S/N) ratio, but more current also spreads the beam due to mutual repulsion of the electrons, reducing sensitivity. To maximize sensitivity, we use a sheet of electrons from a line source, rather than a pencil-like beam from a point source.

Fig. 1 shows the SEEF sensor concept of operation. A heated cathode at the bottom of the sensor thermionically emits electrons from all of its surfaces, in all directions. A pair of steering electrodes biased at + 1 to + 20 V draws electrons upward to form a sheet of electrons headed toward the anodes. Some electrons are collected by the steering electrodes. The remaining electrons return to the cathode. A symmetrical pair of anodes 2000 μm away, biased at + 100 V, collects the electrons. In the absence of an external electric field, the electron currents collected at the anodes are approximately equal.

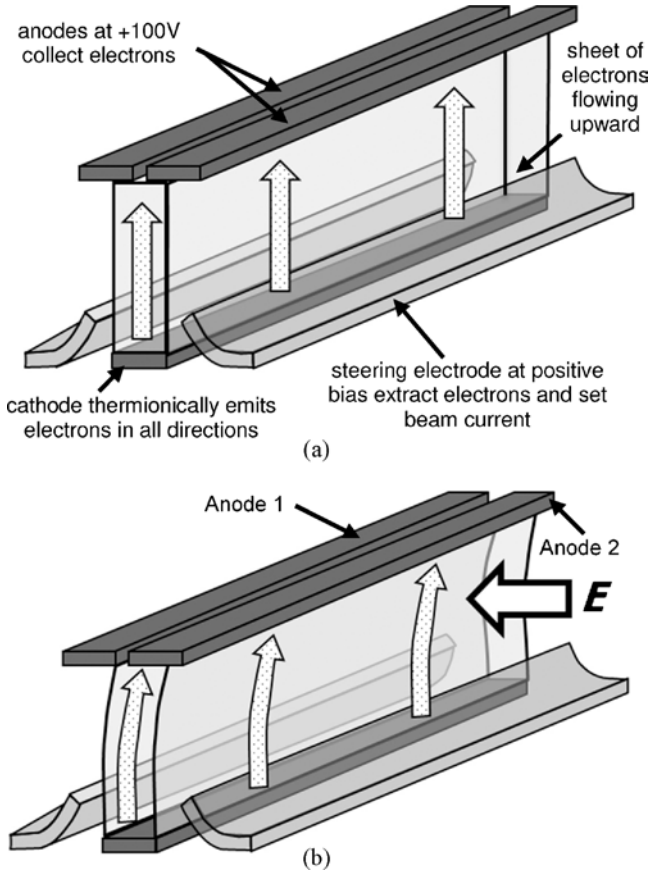

Fig. 1. SEEF sensor concept of operation. (a) Cathode emits electrons and the steering electrodes form them into a sheet. Without an external electric field, the currents collected at the two anodes are approximately the same. (b) With an external electric field perpendicular to the sheet, pointing to the left, electrons are steered to the right. The current on anode 2 increases and that on anode 1 decreases by the same amount.

In practice, there is an unintentional offset due to imperfections in the symmetry, local surface charge, and DC fields.

As seen in Fig. 1(b), with an external electric field transverse to the sheet pointing to the left, the sheet of electrons is steered to the right, reducing the current on one anode and increasing it on the other anode by the same amount. The field is proportional to the difference in anode currents. Taking the difference has the advantage that most of the common-mode noise is subtracted out.

B. Sensor Structure

Most of the SEEF sensor is constructed from dielectrics—glasses and ceramics—because they do not block the electric fields to be detected.

For efficient heating of the cathode, it is constructed as a freestanding bridge over a cavity in a glass chip (see Figs. 2 and 3). This way, conductive heat loss is only at the ends of the bridge. The steering electrodes are fabricated on the same glass chip.

The anodes are fabricated on the underside of another glass chip (see Figs. 3 and 4). Bond pads on the top of the anode chip make contact to the anodes using tungsten vias through the glass.

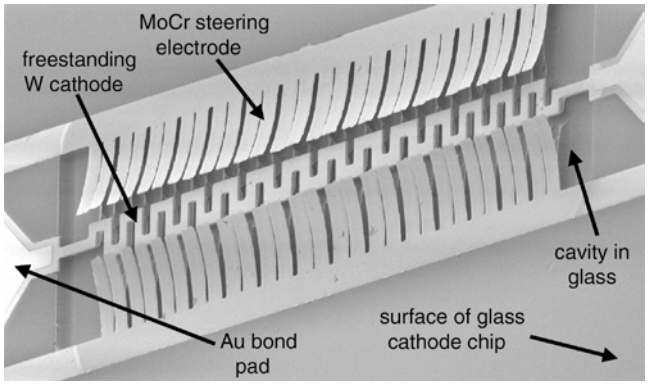

Fig. 2. SEM of cathode chip showing the tungsten cathode and MoCr steering electrodes suspended over a cavity in a glass chip (this cathode does not have an oxide coating).

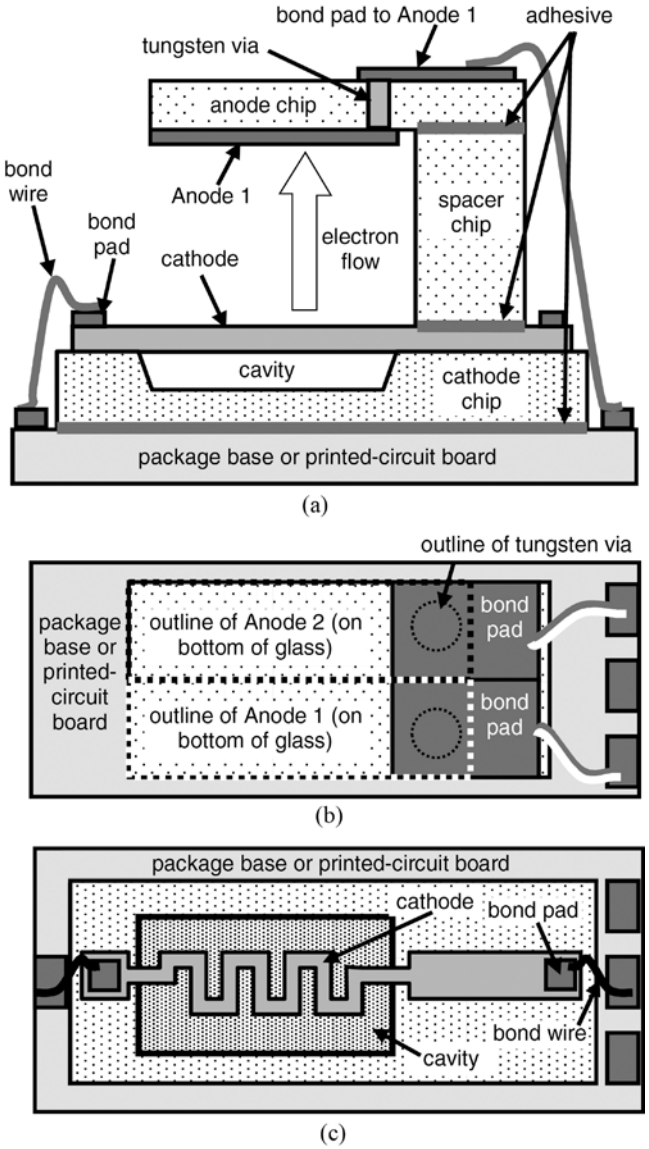

Fig. 3. Drawings of an SEEF-sensor structure. (a) Side view of an SEEF sensor (steering electrodes not shown). (b) Top view showing the anode chip. (c) Top view of the cathode chip by itself (steering electrodes not shown).

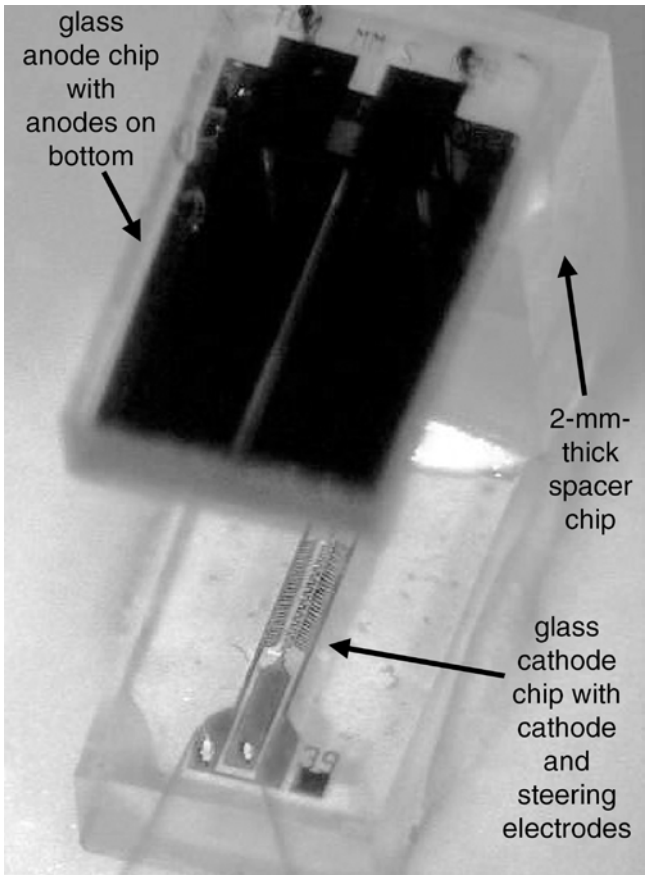

Fig. 4. Photograph showing stack of three glass chips: 1) cathode chip on the bottom, 2) spacer chip in the middle, and 3) anode chip on the top.

The anode chip is held 2 mm above the cathode chip by an unpatterned spacer chip (see Figs. 3 and 4). The three layers are held together with an inorganic adhesive. The same adhesive is used to attach the chip stack to ceramic packages.

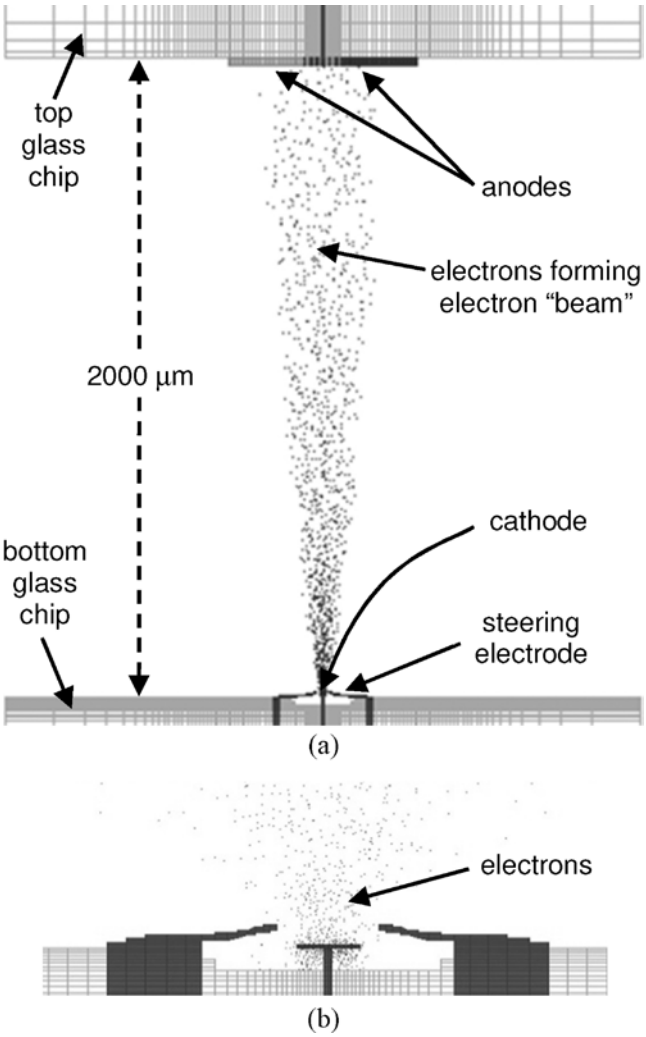

Fig. 5. Two-dimensional electron-flow simulation using MAGIC 2D. (a) Electron-flow region. (b) Closeup of the cathode region. Most emitted electrons return to the cathode.

III. Performance Modeling

Computer simulations and calculations are used to predict and optimize the performance of the SEEF sensor.

A. Electron-Flow Modeling

For electron-flow simulations, we use the particle-in-cell software MAGIC 2D from ATK Mission Systems, which is intended for modeling plasmas. Modeling electrons flowing through a vacuum with voltages applied to conductors is a simple subset of plasma simulation. Because the sensor structure is uniform along the length of the cathode, a 2-D cross section perpendicular to the cathode can be modeled (see Fig. 5). The goal of this modeling is to maximize sensitivity by forming a narrow, high-current electron sheet.

A shortcoming of the software for modeling the SEEF sensor is that surface charge is not modeled: electrons that land on a dielectric disappear from the simulation, when in reality, they create surface charge. Ideally, the simulations would capture this effect, which would result in a local negative potential, which then would repel electrons that later approach the surface. Also useful would be modeling of bleeding off the charge due to surface and bulk conduction in the dielectric.

In thermionic emission, electrons have a distribution of energies in the x-, y-, and z-directions. The average energy perpendicular to the emission surface is kT, and in the two directions parallel to the surface is $\frac{1}{2}kT$ each, where k is Boltzmann's constant and T is the absolute temperature [5]. In these simulations, the thermionically emitted electrons from the cathode fit these distributions.

At a temperature of 1100 K, $\frac{1}{2}kT$ might seem to be insignificant at only 0.047 eV. Due to the small mass of the electrons, however, this energy corresponds to sideways velocity of 130 km/s. This initial velocity is one of the two contributors to electron-beam spreading.

The other cause of beam spreading is mutual repulsion of the electrons. At low emission-current densities, mutual repulsion has a negligible effect. Simulations show that when the current density rises to about 5000 A/m^2, the beam starts to spread more than it already does at lower current

densities. To maximize sensitivity, the current density is limited to this value. For a cathode with a uniformly heated region approximately 600 μm long and 10 μm wide, this yields an emission current from the top of the cathode of about 30 μA.

In vacuum electronics, when a relatively large density of electrons is emitted from a cathode, the high negative space charge causes a local negative potential near the cathode. The minimum in the potential-versus-distance curve is referred to as the virtual cathode. In the SEEF sensor, due to the formation of the virtual cathode, some of the electrons emitted from the cathode travel up a short distance, then return to the cathode [5], [6]. Other electrons are collected by the steering electrodes due to their positive bias. Ten to 20 μA of electron current reaches the anodes.

During the initial design of the sensor, a range of cathode-to-anode spacings L, anode widths, cathode widths, cathode-to-steering-electrode spacings, anode voltages V_A relative to the cathode, and steering-electrode voltages were simulated with MAGIC. The upper voltage limit was set as 100 V, corresponding to the maximum output from many power supplies. The best sensitivity was obtained with $L = 2$ mm. Larger spacings produce more beam deflection, which improves the sensitivity, but also more beam spreading, which degrades the sensitivity even more.

B. Frequency Response

The electron transit time t_t from cathode to anode, neglecting initial velocity, can be calculated from first principles and is given by

$$t_t = [(2m_e)/(V_A e)]^{1/2} L \tag{1}$$

where m_e is the electron mass and e is the electron charge. At $V_A = 100$ V and $L = 2$ mm, $t_t = 0.67$ ns, which corresponds to a maximum operating frequency of 740 MHz for the sensor. There is no theoretical lower frequency limit.

C. Beam Shift

The lateral beam shift Δy due to an external field E_y, again neglecting initial velocity, is given by

$$\Delta_y = E_y L^2 / V_A. \tag{2}$$

D. Electric Fields Through the Sensor

Due to the metal components in the sensor, not all external electric field lines will pass through it. By applying a transverse field to the sensor in a finite-element method (FEM) simulation using the software package ANSYS Multiphysics (SAS IP, Inc.), the field strength along the centerline can be modeled (see Fig. 6). The effect on reducing the beam shift from the metal-free case is modeled by dividing the electron transit time up into 20-ps time increments, calculating the electron distance from the cathode at each time (assuming zero initial velocity), noting the lateral electric field from Fig. 6 at that location, calculating the increase in lateral velocity from the field during the time increment, calculating the lateral shift during the time increment, and finally summing the lateral shifts during the full transport time.

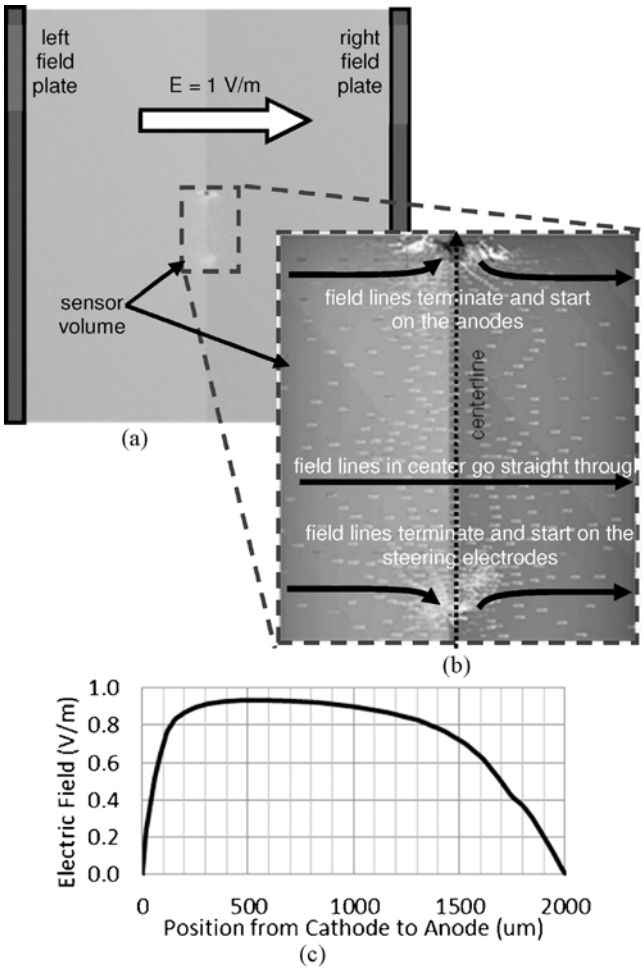

Fig. 6. FEM simulation of electric fields inside of an SEEF sensor. (a) Voltage is applied across external field plates, generating a uniform transverse electric field of 1 V/m. (b) Close-up of the sensor volume. Field lines near the metal steering electrodes, cathode, and anode terminate and start on the metal, while field lines near the center of the sensor pass straight through. (c) Transverse field strength along the centerline of the sensor, from cathode to anode. The field is zero at both ends, and near the external value of 1 V/m in the central region.

Dividing the lateral shift in the sensor by the shift in the metal-free case, the field derating factor f_e is obtained. It varies with the sensor design, being 0.72 for the one modeled here.

E. Beam Spreading and Beam Density

As discussed earlier, as the electron beam travels from the cathode to the anode, it spreads. Beam spreading cannot be calculated, but can be estimated from the electron-flow simulations (cf., Fig. 5) by noting the current in 5-μm-wide sections of anode, as well as current for the entire anode. Dividing the current in each section by the full anode current yields the percentage of current in that section. Dividing the percentage by the section width gives the density D in percent of electrons in the beam per micrometer of anode width. D is at a maximum at the junction of the anodes, falling off slowly tens of micrometers away from the centerline. For the sensor modeled here, $D = 0.44\%/\mu$m.

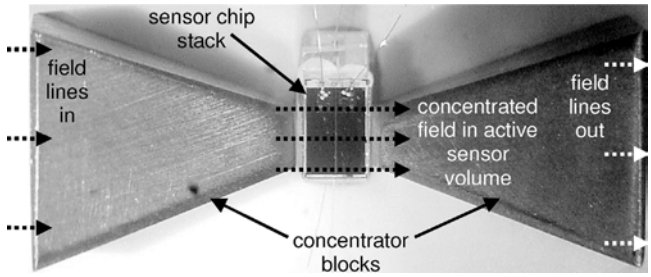

Fig. 7. Top view photograph of SEEF sensor chip stack and metal field concentrator blocks. The ends of the blocks are 2 mm apart and produce a 3.1 × increase in field strength.

F. Electric-Field Concentration

The sensor response can be increased by using wedge-shaped blocks of material to concentrate electric-field lines into the active volume of the sensor, similar to what is done in some magnetic-field sensors [7]. In magnetic-field sensors, a high-permeability material is used; in electric-field sensors, a high-permittivity material such as a dense glass can be used. For the purpose of electric-field concentration, metals effectively act as infinite-permittivity materials and are used for the SEEF sensor.

FEM analysis was used to optimize the shape of the concentrator blocks, which are wedges tapered in two dimensions, and truncated, rather than sharp, at the ends (see Fig. 7). Placing the concentrator blocks as close together as possible, consistent with operation and fabrication of the sensor, optimizes field concentration. The final design has the blocks 2 mm apart and results in a 3.1 × increase in field strength over the case without concentrators. This is captured in the use of another factor, f_c.

The metal concentrator blocks are floating electrically. When the sensor is first turned on, they charge negative due to sideways-directed electrons. This is a self-limiting process: when the concentrators are charged sufficiently negative, subsequent electrons are repelled. The negative charge on the concentrators also helps to reduce the spread of the electron beam.

G. Sensor Response

We define the measured responsivity R_{meas} of the sensor as the ratio of the fractional anode-current difference to the electric field, or

$$R_{\text{meas}} = (2\Delta I_A / I_{\text{A,tot}})/E_y \tag{3}$$

where $I_{A,tot}$ is the total anode current (to both anodes) and ΔI_A is the current shifted from one anode to the other (so the difference in currents is $2\Delta I_A$). The fractional current change, rather than the absolute current change, is used to normalize the responsivity in case of drift in the total anode current. R_{meas} can be measured with a sensor in operation. Using (2) and (3), the definition of D, and the two field factors f_e and f_c, the modeled responsivity can be calculated from

$$R_{\text{model}} = 2L^2 f_e f_c D/V_A. \tag{4}$$

Using the aforementioned values in (4), $R_{\text{model}} = 7.9 \times 10^{-4}$ m/V.

From (4), it would appear that maximizing the cathode-to-anode spacing L and minimizing the voltage V_A would maximize the responsivity. There is a limit to this approach, as each causes the electron density D to drop nonlinearly (this is observed in electron-flow simulations). For significant deviations from the operating point we are using (e.g., reducing V_A from 100 V down to 50 V), the responsivity falls.

H. Noise, Limit of Detection (LOD), and Sensitivity

The LOD occurs when the difference in anode currents $2\Delta I_A$ is not distinguishable from noise. There are four main noise sources: 1) shot noise from the electron current; 2) $1/f$ noise from the electron-emission process and in the detection circuitry; 3) amplifier noise, and 4) digitizer noise. Each is discussed below.

1) *Shot Noise:* Shot noise is due to random variations in the electron current. The shot noise spectral density $i_{\text{shot}}/\Delta f^{1/2}$ is given by

$$i_{\text{shot}}/\Delta f^{1/2} = (2eI_A)^{1/2} \tag{5}$$

where I_A is one anode current and Δf is the bandwidth [8]. Shot noise is white noise, the same at all frequencies of interest. At an anode current I_{A1} or I_{A2} of 10 μA, $i_{\text{shot}}/\Delta f^{1/2} = 1790$ fA/Hz$^{1/2}$.

2) *1/f Noise:* $1/f$, or flicker, noise is from variations in the electron-emission process at the cathode [6] and in the detection circuitry. There is no theory to predict $1/f$ noise as there is for other noise types. In general, below some corner frequency, it rises with decreasing frequency at a rate proportional to I_A^a/f^b, where the exponent a is in the range of 0.5 to 2 and the exponent b is near 1 [8]. In the SEEF sensor, $1/f$ noise becomes significant relative to shot noise below about 10 kHz.

When $1/f$ noise is due to emission, some of the $1/f$ noise is coherent (common mode) at the anodes. Measurements show that taking the difference in anode currents cancels out a significant portion of this noise in the 100-Hz range.

3) *Circuit Noise:* To convert the two anode currents to voltages, a pair of simple op-amp transimpedance amplifiers is used, each followed by 1X op-amp buffers (see Fig. 8) [9]. Op-amps vary greatly in their specifications for input-referred noise voltage and noise current, so they must be selected for the application. For this application, Burr-Brown OPA602 op-amps (Texas Instruments Tucson Corporation) [10] provided the best calculated performance of all the op-amps studied for the transimpedance amplifier circuit using a 500-kΩ feedback resistor. The resistor used is a metal-film resistor, which does not contribute additional $1/f$ noise [8]. The calculated input-referred circuit noise [11], which is dominated by the feedback resistor's Johnson (thermal) noise, is 184 fA/Hz$^{1/2}$ above 1 kHz, up to the bandwidth of the op-amp. At lower frequencies, there is a small, additional $1/f$ noise contribution from the op-amps, rising to an estimated 195 fA/Hz$^{1/2}$ at 1 Hz. Because the different noise sources are added in quadrature, the noise added by the transimpedance amplifier is insignificant compared to the shot noise calculated earlier. The noise added by the 1X buffer is also negligible.

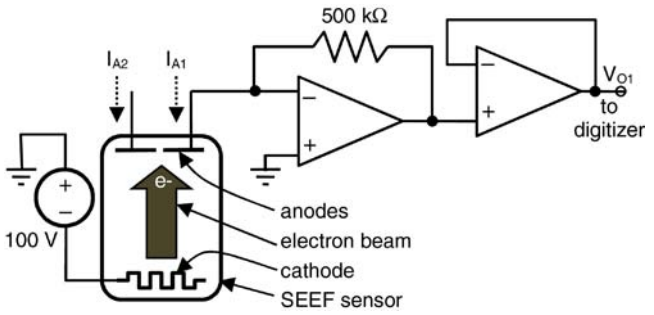

Fig. 8. SEEF sensor and one amplifier circuit (the other is not shown). Each anode current (I_{A1} and I_{A2}) feeds a transimpedance amplifier, followed by a 1X buffer, which drives the digitizer.

4) *Digitizer Noise:* After amplification, the modeled output noise in each channel is $V_{O1,n} = V_{O2,n} = 900$ nV/Hz$^{1/2}$ at 1 Hz and up. The digitizer used, a National Instruments model PXI-5922, contributes noise that is negligible compared to this at 100 Hz and up. The digitizer noise at low frequencies turns out to be small compared to the sensor $1/f$ noise.

5) *Noise Difference:* The signal of interest is the difference in amplified output signals, $V_{O1} - V_{O2}$ (see Fig. 8). For incoherent noises of equal magnitude, when one is subtracted from the other, the noises add in quadrature. This yields an output noise of 1.3 μV/Hz$^{1/2}$ at 100 Hz and up, and 1.7 μV/Hz$^{1/2}$ at 10 Hz. Referred back to the input, this corresponds to a noise of 2.6 pA/ Hz$^{1/2}$ at 100 Hz and up. With a 1-Hz bandwidth, the input-referred, modeled current-difference noise is $\Delta I_{A,noise,model} = 2.6$ pA at 100 Hz and up.

6) *LOD and Sensitivity:* The modeled input-referred noise determines the modeled LOD $E_{y,LOD,model}$. Combining (3) and (4)

$$E_{y,\mathrm{LOD,model}} = (2\Delta I_{\mathrm{A,noise,model}}/I_{\mathrm{A,tot}})/R_{\mathrm{model}}. \quad (6)$$

Using the previously mentioned values in (6), $E_{y,LOD} =$ 0.33 mV/m with a 1-Hz bandwidth, neglecting $1/f$ noise.

Sensor sensitivities are normally written in terms of bandwidth, because a wider bandwidth results in more noise. The modeled sensitivity S_{model} is given by

$$S_{\mathrm{model}} = E_{y,\mathrm{LOD,model}}/\Delta f^{1/2} \quad (7)$$

which calculates out to 0.33 mV/m · Hz$^{1/2}$, neglecting $1/f$ noise. As will be seen from measured data, $1/f$ noise raises the noise floor and, hence, the sensitivity value at frequencies below about 10 kHz.

I. Cathode Design and Modeling

The goals of the cathode design are to emit a sheet of electrons of uniform current density, emit a relatively high current, consume low power, not move when heated, and have long operating life.

Emitting a relatively high current is accomplished by using a line electron source, rather than a point source. As seen in Fig. 9, by gradually widening the cathode filament from the clamped ends to the center, the temperature profile can be made relatively uniform near the center. A uniform temperature produces uniform thermionic emission.

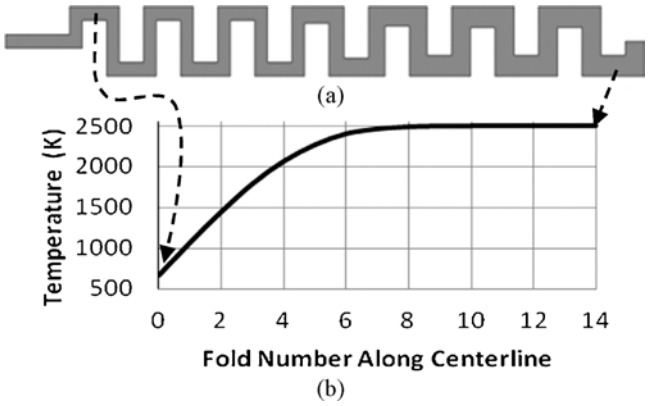

Fig. 9. FEM temperature modeling of half a cathode filament (the cathode is symmetrical). (a) Filament 1000 μm long with width varying from 10 μm at the ends to 14 μm in the center. (b) Temperature simulation result: the profile is fairly flat near the center, resulting in more-uniform thermionic emission. (This result is for an uncoated cathode, which runs at a much higher temperature than an oxide-coated cathode.)

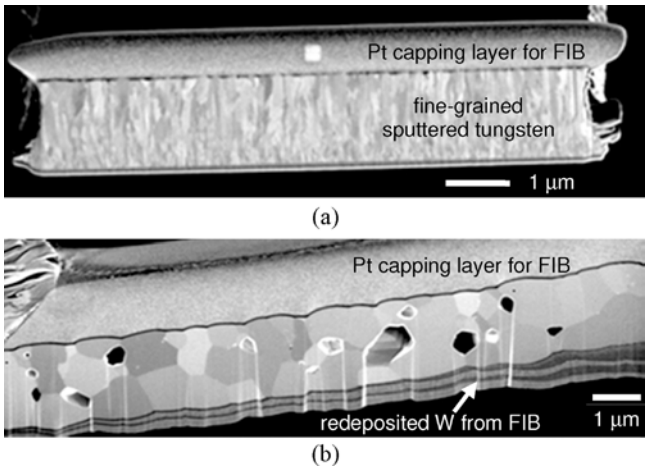

Fig. 10. SEMs of filament cross sections, after depositing platinum on top and cutting with a focused ion beam. (a) As-deposited tungsten, showing fine grains. (b) After heating, grains have grown to the 1-μm range. Large voids have also formed.

Longer filaments are more efficient with power than shorter ones due to the longer thermal path through which heat from the hot center is conducted. A combination of FEM simulations and fabrication and testing of filaments of different lengths led to the choice of 1000 μm as the length of choice.

Structural stability was an issue with several earlier cathode filament designs that operated at temperatures on the order of 2000 to 2500 K. This is because the tungsten, as sputtered, has very fine columnar grains; little microstructure is visible in scanning-electron microscope images (SEMs) of filament cross sections (see Fig. 10). After heating, SEMs show that large grains—many over 1 μm across—form, along with voids. As the grains grow and voids form, bending in random directions occurs at different sections of the filament. Early filament designs with large stress-relief folds bent and twisted severely tens of micrometers out of their original positions, moving the electron emission from its designed location. The solution has two parts: 1) using a design with small folds [cf., Fig. 9(a)], which is stiffer out of plane, and

2) coating the filament with a low-work-function oxide coating, enabling lower temperature operation. Lower temperature cathode operation also lowers the heating power.

IV. Fabrication

Three glass wafers are fabricated separately, then diced and assembled into the three-layer stack to form the SEEF sensor. The bottom layer contains the cathode, the middle layer is a spacer, and the top layer contains the anodes.

A. Bottom (Cathode) Layer

Fabrication of the bottom layer starts with a 1-mm-thick, double-side-polished, soda-lime glass wafer (see Figs. 2 and 3). An insulating material is required to avoid blocking the electric fields to be detected, and glass is suitable for micromachining. 1 mm is for sufficiently thick for good mechanical strength during handling. Soda-lime glass, which contains SiO_2, Na_2O, and CaO [12], is selected over other glasses because it etches faster in 6:1 buffered hydrofluoric acid (BHF) at 560 nm/min [13]. This is convenient because it allows the use of photoresist as the cavity etch mask. For long etch times, the photoresist is not etched, but it tends to peel off in HF solutions.

For the cathode filament, a 20-nm MoCr adhesion layer is sputtered, followed by 4 μm of low-stress tungsten containing 2% La_2O_3 as a low-work-function component. Using a low-stress film avoids peeling when the film is relatively thick, as it is here.

Due to the thick tungsten layer, a hard mask is required for plasma etching, and a thin layer of gold on titanium is used. The sputtered Au/Ti is masked with photoresist and wet etched, followed by plasma etching the W in an $SF_6 + O_2$ plasma.

The steering electrodes are fabricated next. A 1.4-μm layer of image-reversed photoresist is patterned, then 0.9 μm of 85Mo/15Cr is sputtered on. The bottom half of the MoCr is sputtered with a compressive stress of –250 MPa, while the top half has a tensile stress of + 250 MPa. (Stress in many sputtered transition-metal films can be varied by varying the sputter power and pressure. Here, the compressive MoCr was sputtered at a lower pressure than the tensile MoCr.) The MoCr is patterned by lifting off resist in acetone. At this point, the steering electrodes are still flat, stuck down to the glass wafer.

For the bond pads, 6 nm of MoCr is sputtered for an adhesion layer, followed by 0.25 μm of gold. These metals are patterned with photoresist, then wet etched.

Finally, the cavity is formed under the cathode filament and steering electrodes by patterning with photoresist and etching 20 μm into the soda-lime glass in 6:1 BHF. The BHF etch products of soda-lime glass are not all soluble: crystal-like debris, perhaps CaF_2, is left behind. A short exposure to an oxygen plasma, followed by a short etch in nitric acid, removes the debris without damaging the structures on the wafer.

After release, the micromachined structures appear as in Fig. 2. Due to the stress gradient in the steering-electrode fingers, they curl upward upon release.

Before dicing, the top of the wafer is spray-coated with photoresist to protect it. The wafer is cut with a dicing saw into 2 mm × 5 mm chips and the debris is rinsed off with water. Finally, the photoresist is stripped in an oxygen plasma (not using a wet stripper avoids stiction problems).

B. Mounting Bottom Chip and Coating Cathode

Alumina package bases were made to specification by Advanced Technical Ceramics. To repeatably achieve a high bond strength to the glass chips, the packages are cleaned in an oxygen plasma before use.

A 50- to 200-μm-thick layer of Ceramabond 503 (Aremco Products, Inc.) alumina adhesive is applied to the ceramic base. A cathode chip is placed and the adhesive is cured at up to 400 °C in a vacuum oven. The vacuum avoids any undesired oxidation of the metals present. After curing, this can tolerate exposure to temperatures of over 500 °C, which is useful later in the process for vacuum packaging. Finally, wires bonds are made from the cathode and steering-electrode pads to the package.

C. Coating Cathode With Low-Work-Function Layer

The cathodes are coated with a low-work-function layer comprised of BaO/SrO/CaO (referred to as oxide) to enable operation at around 1100 K [6]. This is a relatively low temperature compared to what would be needed using tungsten with lanthanum or pure tungsten, and avoids the cathode deformation problem discussed in Section III.I.

BaO/SrO/CaO is rapidly degraded when exposed to the atmosphere. To avoid this, its use requires a multistep process. Coating starts with the electrical plating of about 2 μm of fine particles of $BaCO_3/SrCO_3/CaCO_3$ (referred to as tricarbonate) onto the tungsten filament. The tricarbonate particles are protected by coatings of polyvinyl acetate and suspended in acetone during plating. The tricarbonate is converted to oxide later during the vacuum sealing process.

D. Middle (Spacer) Layer

The starting material for the middle layer of glass is a 2-mm-thick Borofloat (Schott AG) glass wafer. No patterning is done on the wafer. Cuts are made with a dicing saw set to create rectangular blocks of 1.6 mm × 2 mm. Due to the thickness of the glass, it is cut in two passes, each 1 mm deep.

E. Top (Anode) Layer

Fabrication of the top layer starts with a 0.5-mm-thick Schott HermeS wafer, which has predefined groups of six tungsten-wire vias in an array across a Schott Borofloat B33 wafer (see Fig. 11). Each group of vias is used for one anode chip. The chips on the anode wafer are laid out to align to the vias.

On the top side of the wafer, 9 nm of MoCr is sputtered for an adhesion layer, followed by 0.25 μm gold for the bond pads. On the bottom side, the same MoCr and gold layers are sputtered for the anodes. The top-side metals are patterned and wet etched to form the bond pads, while protecting the bottom metals. The bottom-side metals are then patterned and etched to form the anodes while protecting the top [see Fig. 3(a)]. Finally, the wafer is diced to form the top-layer chips.

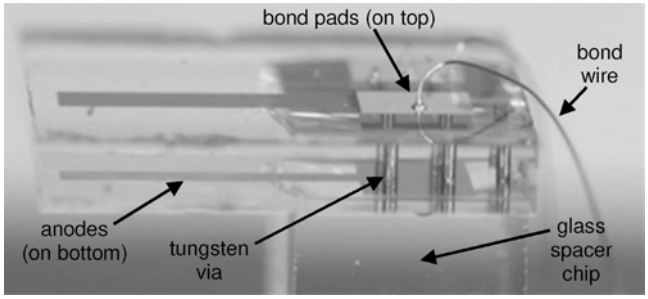

Fig. 11. Top glass layer containing gold anodes on the bottom, tungsten vias, and gold bond pads on top.

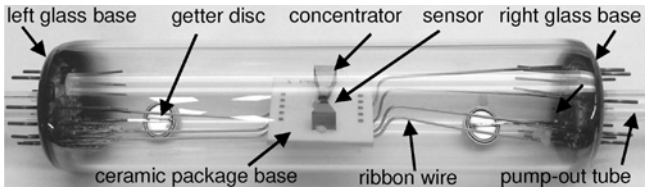

Fig. 12. SEEF sensor sealed inside of a glass vacuum tube.

F. Mounting Top and Middle Chips and Concentrators

The top and middle chips are bonded together with Ceramabond 503 adhesive, then aligned to the bottom chip with a die-attach tool and bonded with the same adhesive. Wire bonds are made from the anode pads on the top chip to the package. Finally, field concentrators are mounted on the sides of the chip stack (see Fig. 7). The concentrators are made of Kovar (CRS Holdings, Inc.) for a good thermal-expansion-rate match to the alumina base.

V. Vacuum Packaging and Oxide Activation

As previously discussed, the glass sensor chip stacks are mounted on ceramic package bases. The long-term goal is to vacuum seal the sensor using a ceramic lid bonded on with glass frit. As a lower risk path to vacuum packaging, glass tubes are used, as described here.

Ribbon wires are resistance welded from the pins on the left side of the ceramic base to pins on an off-the-shelf glass base (see Fig. 12). The same is done on the right side with another base (running the wires to both sides, rather than all to one base with wires under the sensor, produces better sensitivity). Getter disks are also attached to each base. A glass tube, 150 mm long and 39 mm in diameter, encloses the wires and ceramic base. The tube is fused to the two glass bases with a propane torch.

At this point, the inside of the tube is at atmospheric pressure. One of the glass bases has a narrow pump-out tube extending from it, which is connected to a high-vacuum pump and pumped to below 1×10^{-5} Torr. Following a standard process in the vacuum-tube industry [14], the entire structure is then heated to 400 °C and pumped out for over 12 h, reducing the pressure down to the 10^{-7}-Torr range. Upon cooling, the pressure drops further.

While still on the vacuum pump, a slowly increasing current is flowed through the cathode filament, gradually heating it.

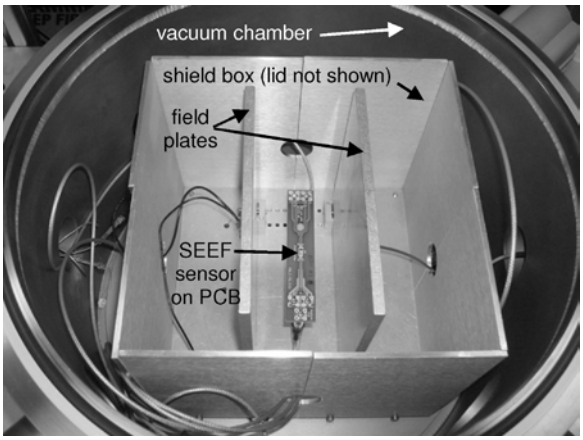

Fig. 13. Vacuum test system. Here, the SEEF sensor is mounted on a PCB.

The binder is first burned off, which causes a tiny, momentary pressure spike. The cathode is further heated to the 1100-K range, at which it is just visible to the naked eye as a reddish-orange glow. At this temperature, the tricarbonate coating is converted to the oxides (BaO/SrO/CaO). A positive voltage applied to the anodes is used to check that the cathode is emitting electrons.

Next, a section of the pump-out tube is heated to the working range of the glass [12]. The external atmospheric air pressure collapses the pump-out tube and forms a seal.

In the absence of a getter, the pressure inside the tube will gradually rise due to outgassing and leakage. The industry-standard method of dealing with this is the use of a getter, which binds to most gas species (other than the noble gases), locking them in a solid form away from the sensor. Here, the disk getters are activated by radio frequency heating through the tube wall, which initiates a reaction that releases a vapor of metallic barium [15]. The barium forms a dark-colored film on the nearby glass wall, which getters for the life of the tube.

VI. Test System

The vacuum test system seen in Fig. 13 is comprised of a vacuum chamber with electrical feedthroughs, a shield box inside the chamber, parallel field-generation plates, a plastic post to hold the sensor near the center of the plates, and coaxial cables for the sensor and field plates. At 150 mm square, the plates are larger than the 62-mm spacing. When a voltage is applied to the plates, the electric field generated is uniform away from the edges, as confirmed by testing with a Model 100 D field probe from Beehive Electronics.

The vacuum chamber, which can reach the 10^{-7}-Torr range, is used for testing unpackaged sensors mounted on printed circuit boards (PCBs). Vacuum-packaged sensors are tested in the same system without pumping down.

After the anode currents are amplified and converted to voltages (with a conversion factor of 0.5 MΩ), they are digitized. With a small AC voltage riding on a large DC voltage, as is the case here, the input to a digitizer or oscilloscope is typically AC-coupled, with a typical high-pass corner frequency of 10

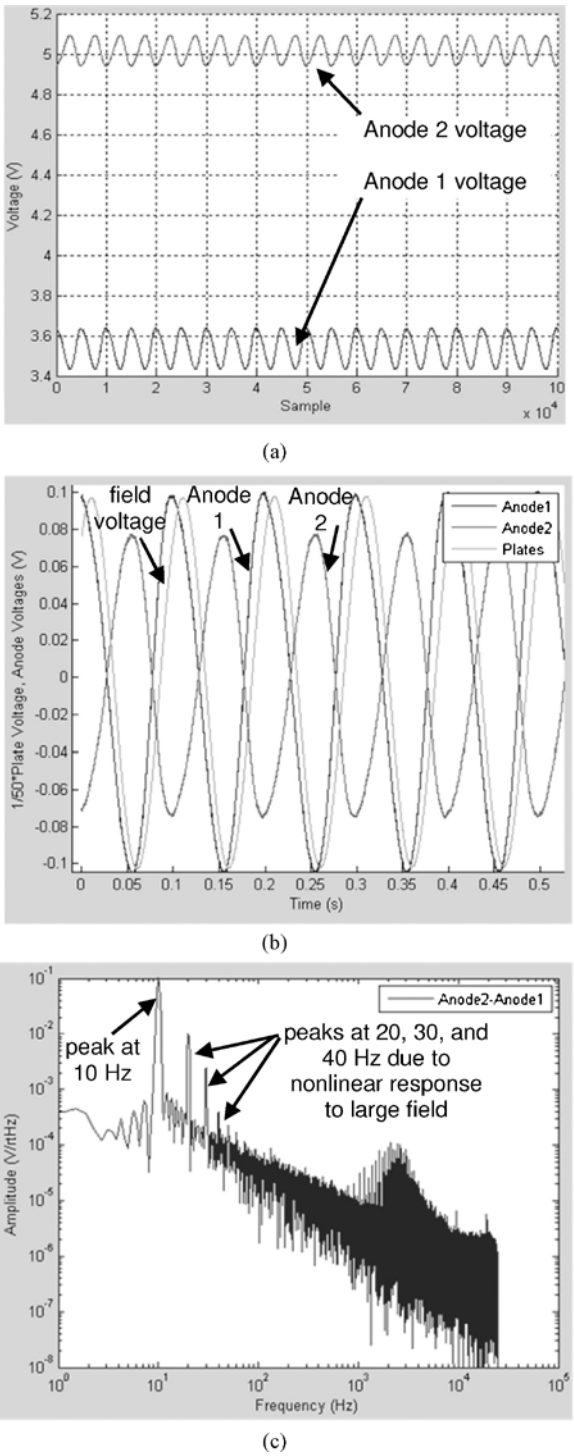

Fig. 14. Sensor data with field of 81 V/m zero to peak at 10 Hz. (a) Raw voltage data of amplified anode currents at 50 kS/s. (b) Applied plate voltage to generate the field and amplified anode voltages with DC subtracted off versus time. A LabVIEW timing issue causes the time offset between the applied field and the response. (c) Spectrum of the difference in anode voltages. The y-axis units are V/Hz$^{1/2}$. 1/f noise is the dominant noise below 10 kHz.

to 90 Hz. For detection of low-frequency fields, AC coupling would filter out the signal to be detected. A solution is to use DC coupling and a high-resolution digitizer. Here, we use a National Instruments PXI-5922 digitizer, which has two channels, set to ± 5.1 V full scale input, running at 50 kS/s, with a resolution of 24 bits. Data acquisition is controlled by a LabVIEW (National Instruments Corporation) program.

VII. Results

In this section, results for unsealed sensors operated in the pumped vacuum chamber and packaged sensors operated in a vacuum tube are presented.

A. Unsealed SEEF Sensor

In operation, the steering electrodes are typically set to 10 V. A voltage is applied across the cathode and ramped up until there is about 20 μA total anode current. At this operating point, the cathode voltage and current are typically 0.5 V and 40 mA, for a heating power of 20 mW. The anode currents consume another 2 mW of power, for a total of 22 mW to operate the sensor.

Fig. 14(a) shows raw sensor output data with an applied electric field of 81 V/m zero-to-peak at 10 Hz. The amplified anode voltages are not equal; there is a noticeable DC offset. Fig. 14(b) shows the voltage applied to the field plates and the anode voltages with the DC values subtracted off. The graph shows a small time offset between the field voltage and the sensor response, due to a timing issue in the LabVIEW program controlling two different digitizers; anode 1 actually operates in phase with the field. As expected from the design, anodes 1 and 2 are 180° out of phase. Anode 1 has a greater voltage swing than anode 2, implying that some of the change in electron-beam current is going somewhere other than the anodes. Because the sensor is in the vacuum chamber surrounded by the field plates and shield box, these could be collecting electrons. Fig. 14(c) shows a spectrum of the difference in anode voltages, generated using a discrete time transform in MATLAB (The MathWorks, Inc.). There is a large peak at 10 Hz, as well as smaller peaks at the harmonic frequencies. Harmonic peaks are seen with the SEEF sensor for larger input fields.

The measured sensor responsivity R_{meas}, calculated from (3) and the data in Fig. 14, is 2.4×10^{-4} m/V, which is about a third of modeled result from (4). Possible reasons for the difference are the inability to include surface charge in the model, too coarse of a time resolution for the field-derating factor f_e, not accounting for initial electron velocity in (4), and not including the metal lines in the PCB in the simulation in Fig. 6.

Data were taken at frequencies of 1 Hz, 10 Hz, 100 Hz, 1 kHz, and 10 kHz. Above 100 kHz, capacitive coupling from the field plates to the metal lines in the sensor and test system generates currents 90° out of phase with the plate voltage, which completely overwhelms the signal from the anode currents. The fields range from 81 V/m, the maximum that could be applied with a function generator outputting 5 V zero-to-peak, down to 4 mV/m, for the smallest field that could be detected at 10 kHz. Data were taken for a duration of 0.1 s at 10 kHz, and for 0.5–2 s at the other frequencies. The bandwidth Δf is the inverse of the sampling time (e.g., 1 s of sampling corresponds to a 1-Hz bandwidth).

TABLE I
SENSITIVITIES VERSUS FREQUENCY FOR UNSEALED AND SEALED SENSORS

Frequency (Hz)	*Sensitivity for Unsealed Sensor* (mV/m · $Hz^{1/2}$)	*Sensitivity for Sealed Sensor* (mV/m · $Hz^{1/2}$)
1	134	
10	34	470
100	6.3	230
1000	2.4	140
10 000	0.39	

To determine the LOD at each frequency, spectra are observed for the lowest field that produces a frequency peak clearly visible above the noise. The peak height is divided by the adjacent noise reading to get the S/N ratio. Finally, the applied field is divided by the S/N ratio to obtain the LOD. This is divided by the square root of the bandwidth to calculate the measured sensitivity.

Table I shows the measured sensitivity at each frequency. The sensitivity of 0.39 mV/m · $Hz^{1/2}$ at 10 kHz, where the 1/*f* noise is about the same as the shot noise, compares well to the modeled sensitivity in (7). At lower frequencies, 1/*f* noise increases the sensitivity value.

B. Vacuum-Sealed SEEF Sensor

The SEEF sensor sealed in a vacuum tube in Fig. 12 was tested in the same way as the unsealed sensor. Because it is less sensitive, a peak at 1 Hz could not be seen above the noise. The sensor in the tube has larger wires than the unsealed sensor on a PCB, resulting in capacitive coupling at 10 kHz and up that swamped out the signal.

The measured sensitivities versus frequency are shown in Table I. The sealed sensor is one to two orders of magnitude less sensitive (i.e., it has a higher LOD) than the unsealed sensor. The reason for this is unknown at present, but may be due to electronic surface charge on the glass tube. A potential solution to this would be a mildly conductive coating on the tube. Clearly, there is a tradeoff between controlling surface charge and allowing the external electric field to enter the sensor. A future version of the SEEF sensor in a smaller vacuum package would likely be even more sensitive to such charging effects.

C. Lifetime Testing

One vacuum-sealed test device with an oxide-coated cathode was sealed in a vacuum tube. The cathode was driven so that 10 μA or more current was collected continuously on an anode. The anode current (which tracks the emission current) initially rose for a few days as the oxide was fully activated. The emission current then decayed over the following weeks as the barium, strontium, and calcium sublimated off [6], and dropped to near zero at 31 days (750 h). For many applications, an SEEF sensor would not need to be operated continuously, which could extend the useful lifetime to several years.

VIII. CONCLUSION

We have designed, modeled, fabricated, and tested a new type of low-frequency, low-power electric-field sensor based on deflection of an electron sheet.

Several different modeling methods—finite-element, electron-flow, and calculations with equations from first principles—have been used to predict and optimize the performance of the SEEF sensor. Finite-element analysis was used to increase the length of the electron-emission region of the cathode, which increases sensitivity. Electron-flow simulations were used to get a feel for the electron paths and to narrow the spread of the electron sheet through the use of the steering electrodes. Equations (4) and (6) give a feel for how sensor response and LOD are affected by design and operation variables.

The SEEF sensor was fabricated through a novel process flow that includes stress-controlled W and MoCr films, high-temperature-compatible glass-wafer bonding, low-work-function coatings, and high-vacuum packaging.

The sensor's responsivity was a factor of 3 different than predicted, indicating a good but imperfect model.

For future work, the sensor could be vacuum packaged in a ceramic package containing a getter. For smaller size and lower production cost, the vacuum cavity could be formed from wafer-to-wafer bonding.

ACKNOWLEDGMENT

We thank Dr. L. Currano of the Army Research Laboratory for the cross-sectional cathode SEMs in Fig. 10, and Dr. D. Shenoy for serving as the DARPA program manager.

REFERENCES

[1] A. D. Hibbs, Y. Zhang, L. J. Burnett, D. M. Hull, and S. J. Vinci, "Electric field sensing: Measurement and applications," Aug. 2009, to be published.

[2] M. A. Krupka, R. Matthews, C. Say, A. D. Hibbs, and G. D. Delory, "Development and test of free space electric field sensors with microvolt sensitivity," Quantum Applied Science Research Inc., San Diego, CA, USA, Tech. Rep. AD-A409234, Oct. 2001.

[3] *Photonic Electric Field Sensor System Model 200-04*, SRICO, Inc., Columbus, OH, USA, Jun. 2012.

[4] J. E. Toney, V. E. Stenger, P. Pontius, N. Smith, J. Scholl, A. Pollick, B. Sadani, H. Lu, M.-P. Bernal, and S. Sriram, "Photonic crystal dectro-optic devices in engineered thin film lithium niobate substrates," in *Photonic Microdevices/Microstructures for Sensing IV, Proc. SPIE*, vol. 8376, X. Fan, H. Xiao, and A. Wang, Eds. May 2012, pp. 83760H-1–83760H-12.

[5] K. R. Williams, "Micromachined hot-filament vacuum devices," Ph.D. dissertation, Dept. Elect. Eng. Comput. Sci., Univ. Calif., Berkeley, CA, USA, 1997.

[6] K. R. Spangenberg, *Vacuum Tubes*. New York, NY, USA: McGraw-Hill, 1948, pp. 1–11.

[7] G. A. Fischer and A. S. Edelstein. (2010). Magnetic modeling of a rotating flux concentrator system designed to mitigate noise in 'large' magnetic sensors, Army Research Laboratory, Defense Technical Information Center, Adelphi, MD, USA, Tech. Rep. ARL-TR-5317 [Online]. Available: http://www.dtic.mil/dtic/tr/fulltext/u2/a529158.pdf

[8] P. R. Gray and R. G. Meyer, *Analysis and Design of Analog Integrated Circuits*, 2nd ed. New York, NY, USA: Wiley, 1984, ch. 11.

[9] S. E. Schwarz and W. G. Oldham, *Electrical Engineering: An Introduction*. New York, NY, USA: Holt, 1984, ch. 8.

[10] *OPA602: High-Speed Precision Difet Operational Amplifier*, Burr-Brown Products, Texas Instruments, Dallas, TX, USA, Oct. 2002.

[11] *ADA4898: High Voltage, Low Noise, Low Distortion Unity-Gain Stable, High Speed Op Amp*, Analog Devices, Norwood, MA, USA, 2010.
[12] J. E. Shelby, *Introduction to Glass Science and Technology*, 2nd ed. Cambridge, U.K.: Roy. Soc. Chem., 2005.
[13] K. R. Williams, K. Gupta, and M. Wasilik, "*Etch rates for micromachining processing—Part II*," *J. Microelectromech. Syst.*, vol. 12, no. 6, pp. 761–778, Dec. 2003.
[14] B. Vancil and E. Beam, private communication, Jan. 2012.
[15] SAES Getters S.p.A. (2012). Barium getter features [Online]. Available: http://www.saesgetters.com/default.aspx?idPage = 460
[16] S. Ghionea and D. Hull, "Characterization techniques for a MEMS electric-field sensor in vacuum," in *Proc. Electrostat. Joint Conf.*, Cambridge, ON, Canada, Jun. 12–14, 2012, Paper R3.

Kirt R. Williams (S'90–M'97–SM'01) received the B.S. (Hons.) degree with a double major in electrical engineering and computer sciences (EECS) and materials science and engineering and the M.S. and Ph.D. degrees in EECS, all from the University of California at Berkeley, Berkeley, CA, USA, in 1987, 1993, and 1997, respectively.

He previously designed circuits at Western Digital, developed all-silicon plate valves using a novel thermal actuator at NovaSensor, and did research and development on high-Q variable capacitors and optical switches at Agilent Technologies. From 2004 to 2012, he was involved in research on microelectromechanical system (MEMS), system engineering, and program management at Science Applications International Corporation. He is currently a Principal MEMS Engineer at InvenSense, San Jose, CA, USA.

Dr. Williams is the co-author of *An Introduction to Microelectromechanical Systems Engineering* (2nd ed. Boston, MA, USA: Artech House, 2004) and papers on etch rates for micromachining in the *Journal of Microelectromechanical Systems*. He holds a number of patents related to MEMS devices.

Dirk P. H. De Bruyker (M'09) received the M.Sc. and Ph.D. degrees in electrical engineering from the Katholieke Universiteit Leuven, Leuven, Belgium, in 1994 and 2002, respectively.

He is currently a Senior Staff Scientist at the Palo Alto Research Center (PARC), Palo Alto, CA, USA. He was the inventor of a novel microfluidic mixing technique, the co-inventor of the (at the time) world's smallest pressure sensor, and has acted as a Principal Investigator for PARC on several U.S. government funded projects.

Dr. De Bruyker has more than ten years of experience in MEMS/microsystem design, CAD, and fabrication, published more than 30 peer reviewed articles in the field, and holds several patents.

His research interests range from microspring technology for packaging to optical MEMS (miniaturized optical switches and micromirrors) to biomedical microsystems (bioelectric field sensing and calorimetric enthalpy arrays for proteomics).

Scott J. Limb received the B.S. degree with high honors in chemical engineering from the University of California Berkeley, CA, USA, in 1991, and the Ph.D. degree in chemical engineering from the Massachusetts Institute of Technology, Cambridge, MA, USA, in 1997.

From 1997 to 1998, he was with Tokyo Electron Ltd., as a CVD Process Development Engineer. From 1998 to 2002, he was with the MEMS Division, Analog Devices, where he developed micromachined accelerometers and optical switches. Since 2002, he has been with the Hardware Systems Lab, Palo Alto Research Center, Palo, Alto, CA, USA, as a Senior Researcher.

Eric M. Amendt (M'03) received the B.S. and M.S. degrees in electrical engineering from California Polytechnic State University (Cal Poly), San Luis Obispo, CA, USA, in 2004 and 2007, respectively.

From 2004 to 2005, he was involved in research on sensor systems and algorithms for autonomous navigation for the Defense Advanced Research Projects Agency Grand Challenge at Cal Poly. Since 2005, he has been involved in research on sensor technologies, applied signal and image processing techniques, and modeled sensor phenomenology in the fields of E&M, radar, biology, and multispectral video at Science Applications International Corporation, San Diego, CA, USA. He is the first author of "Image segmentation for off-road autonomous navigation: Multidimensional k-means and statistical image analysis," Signal and Image Processing, IASTED, Kona, HI, USA, August 2008.

Doug A. Overland received the B.S. degree in general engineering from Harvey Mudd College, Claremont, CA, USA, in 1995.

From 1995 to 1997, he was a Lead Electro-Mechanical Engineer at SAIC, developing an automated laboratory system from prototype to first-generation product, where since 2008, he has been involved in the design and construction of instrumentation in support of the Sensor Technology Division. From 1997 to 2008, he was at Amgen, Inc., supporting research and development of novel therapeutics through the design and implementation of custom automation and robotics applications. Mr. Overland is the co-author of "The automatic metric monitoring program" in the *Journal of Laboratory Automation*, vol. 8, pp. 24–27, Feb.–Mar. 2003.